Soft Matter

Journal Name

ARTICLE

Effect of Surface Modification on Interfacial Nanobubble Morphology and Contact Line Tension

Kaushik K. Rangharajan,[a] Kwang J. Kwak,[b] A.T. Conlisk,[a] Yan Wu[c,*] and Shaurya Prakash[a,*]

Past research has confirmed the existence of surface nanobubbles on various hydrophobic substrates (static contact angle > 90°) when imaged in air-equilibrated water. Additionally, use of solvent exchange techniques (based on the difference in saturation levels of air in various solvents) also introduced surface nanobubbles on hydrophilic substrates (static contact angle < 90°). In this work, tapping mode atomic force microscopy was used to image interfacial nanobubbles formed on bulk polycarbonate (static contact angle of 81.1°), bromo-terminated silica (BTS; static contact angle of 85.5°) and fluoro-terminated silica (FTS; static contact angle of 105.3°) surfaces when immersed in air-equilibrated water without solvent exchange. Nanobubbles formed on the above three substrates were characterized on the basis of Laplace pressure, bubble density, and contact line tension. Results reported here show that (1) the Laplace pressures of all nanobubbles formed on both BTS and polycarbonate were an order of magnitude higher than those of FTS, (2) the nanobubble number density per unit area decreased with an increase in substrate contact angle, and (3) the contact line tension of nanobubbles was calculated to be positive for both BTS and polycarbonate (lateral radius, $R_s < 50$ nm for all nanobubbles) and negative for FTS ($R_s > 50$ nm for all nanobubbles). The nanobubble morphology and distribution before and after using the solvent exchange method (ethanol-water), on the bulk polycarbonate substrate was also characterized. Analysis for these polycarbonate surface nanobubbles showed that both the Laplace pressure and nanobubble density reduced by ≈ 98% after ethanol-water exchange, accompanied by a flip in the magnitude of contact line tension from positive (0.19 nN) to negative (–0.11 nN).

Introduction

Interfacial nanobubbles are surface-bound gaseous structures with at least one sub-100 nm dimension that exist on solid surfaces submerged in a liquid, with water being the most common. The presence of nanobubbles and micropancakes [1,2] has been considered critical to many applications such as reducing skin friction/drag on surfaces due to induced hydrodynamic slip,[3-5] foam flotation applications for mineral extraction,[6] heterogeneous cavitation,[7] ultrasound irradiation induced nanobubbles that act as contrast agents for imaging tumors,[8] and reduced surface fouling due to changes in adhesion of a liquid to hydrophobic surfaces.[9]

The existence of nanobubbles is now generally accepted; however, there is still a lack of consensus regarding the mechanisms that keep these bubbles stable for hours to days. [10,11] Furthermore, characterization of these interfacial gaseous structures on chemically modified silica is limited, with only investigation of hydrophobic end-groups reported

(see Table S1, supporting information). Since the reported size of the observed bubbles shows significant variation, the Laplace pressure usually varies over nearly three orders of magnitude (∼ 0.01 – 10 MPa), and therefore under ambient conditions the nanobubbles should be thermodynamically unstable and diffuse out spontaneously.[12] Analytical studies on free energy minimization have shown that nanobubbles cannot be attached in a stable manner to hydrophobic substrates as this leads to a maximization of the thermodynamic potential.[12,13] Thermodynamics also shows that formation of a constant curvature nanobubble at the solid-liquid interface is an energy consuming process and consequently, an open question remains on the role of nanobubble formation in imparting energy stability to the entire liquid-solid-gas interfacial system.[14]

To address the question of nanobubble stability, several hypotheses have been proposed over the years. Mathematical models show that the addition of a constant potential component (with chemical potential being thermodynamically independent of the immersed medium) for the fluid particle

leads to stable attachment of nanobubbles to the substrate.[15] In aqueous solutions, hydrogen bonding present at the nanobubble interface appears to restrict high Laplace pressure-induced diffusivity and thus helps maintain dynamic stability.[16] Models using constrained lattice density functional theory show that intrinsic nanoscale roughness and chemical heterogeneities present in substrates may be responsible for contact line pinning,[17] also leading to stable surface nanobubbles.

Moving away from these fundamental surface science hypotheses, the role of experimental conditions has also been considered. For example, presence of contaminants on the nanobubble surfaces could play a role in reducing interfacial tension between the gas phase and water thereby imparting stability. [14,18-20] Impurities introduced into the system (e.g., impurities formed by the interaction of solvents and/or surfactants with substrate) during the solvent exchange procedure may be yet another reason for observed nanobubble stability.[18] Force curve measurements using an atomic force microscope (AFM) have shown the existence of interfacial gas enrichment layer when solvent exchange was used, which may be responsible for feeding a net influx of gas to the bubble, thus maintaining a dynamic equilibrium.[21] The stability of nanobubbles due to dynamic equilibrium is also supported by the attraction of non-polar gases towards hydrophobic walls[22-25] which alters the liquid structure close to the wall and also reduces the surface tension at the liquid-gas interface.[23] It is important to note that none of the stability mechanisms reported to date have been widely accepted. Recently, a report showed that nanobubble stability can be explained due to a combination of pinning effect and the oversaturation of gas in the system. [26]

Previous reports investigate nanobubbles formed on hydrophobic surfaces including polymer thin films,[4,27-30] functionalized glass and silicon substrates with silane moieties, usually with methyl termination,[31,32] and functionalized gold surfaces using a thiol tether.[33,34] Therefore, for these experimental reports, the static contact angle has varied between 92°–110°.[35,36] Additionally, modified surfaces[37] have been prepared with both vapor and solution-based methods and therefore effects of surface roughness, thickness of surface layers, and order of monolayers have also been evaluated.[37] Of the handful of studies evaluating other than methyl group termination for surface functionalities, a fluorinated surface prepared by vapor deposition from 90% 1H,1H,2H,2H-perfluorodecyldimethylchlorosilane showed spontaneous formation of nanobubble via substrate heating and also reported increase in bubble density with rise in water temperature.[38]

Among hydrophilic substrates (static contact angle < 90°), gold [39,40] and highly ordered/oriented pyrolytic graphite (HOPG) were the imaging surfaces for several nanobubble reports.[11,35,41-47] Most substrates in previous work used the solvent exchange process to introduce nanobubbles on HOPG including use of aqueous electrolytes[44] for subsequent imaging of the nanobubbles. Also, the presence of contaminants from air in contact with gold and freshly cleaved HOPG increases the static contact angle of the substrates thereby giving rise to uncertainties in systematically characterizing the nanobubbles

formed on these substrates.[39,40,48,49] Specifically, several reports show static contact angle of freshly cleaved HOPG varying between $\approx 63° - 91°$.[48-51]

The purpose of this paper is to distinguish and characterize nanobubbles formed on surfaces of varied hydrophobicity. Specifically, one hydrophobic (borosilicate glass functionalized with fluoro termination) and two hydrophilic (bulk, commercially available polycarbonate and borosilicate glass functionalized with a bromo terminated silane) substrates were prepared to systematically characterize and compare nanobubbles formed when the substrates were immersed in air-equilibrated water. The calculated Laplace pressures for the nanobubbles are presented along with the estimated nanobubble density and contact line tension (CLT). Nanobubbles generated via the solvent exchange process were also introduced to compare directly the changes to morphology, CLT, and distribution of nanobubbles in contrast to those generated via air-equilibrated water, for the bulk polycarbonate substrate.

Experimental Methods

Sample Preparation by Surface Modification of Silica Substrates

Functionalization of the borosilicate glass substrates follows from several previous reports showing reliable preparation of surface layers.[52-55] Borosilicate glass disks, 25 mm in diameter (VWR, Chicago, IL) were initially degreased with acetone, isopropanol (IPA), deionized (DI) water (Millipore 18.2 MΩ), and blow-dried using a constant stream of dry, filtered air. Then, the glass disks were placed in a staining rack and sonicated in IPA for 10 min. Following the IPA sonication, excess IPA was removed and the glass disks were cleaned using a piranha solution (4:1 H_2SO_4/H_2O_2 by volume) for 30 min. (Caution: Piranha solution is a strong oxidizing agent and adequate safety measures should be exercised while handling the solution). The glass disks were subsequently rinsed with copious amounts of DI water and dried under a constant stream of dry, filtered air. The samples were then placed on a hot plate at 100°C for 30 min in a glove bag continuously purged with dry N_2 to remove any residual water. After 30 min, the hot plate was switched off and the samples were still kept inside the glove bag and allowed to cool to room temperature.

Surface modification was performed on the glass substrates following previously reported methods[52,53] to introduce a silane monolayer of varying hydrophobicity on a glass substrate in contrast to the self-assembled thiol monolayers[34] on gold substrates. In order to avoid ambient contamination and maintain a clean and controlled environment, all the glassware used to perform surface modification were cleaned with piranha solution and stored inside a clean, enclosed oven maintained at 120°C (to prevent any residual water on surfaces) until use. To obtain bromo-terminated silica (BTS), the clean glass samples were immersed and soaked for two hours inside a solution containing 1% v/v 11-bromoundecyltrichlorosilane (Gelest Inc., Morrisonville, PA) in anhydrous cyclohexane (Sigma-Aldrich, St. Louis, MO). The samples were then rinsed in excess

anhydrous cyclohexane solution followed by a 15 min sonication in excess N,N-dimethylformamide (Sigma-Aldrich, St. Louis, MO). The samples were then dried using a continuous stream of filtered dry air and heated at 80°C using a hot plate for 45 min., with all the aforementioned steps performed in a continuously nitrogen purged glove bag. The samples were stored in an environmentally isolated dry box that was also continuously flushed with nitrogen until further use.

To obtain fluoro-terminated silica (FTS), the clean glass samples were immersed and soaked for two hours in 1% v/v of (heptadecafluoro-1,1,2,2-tetrahydrodecyl)trichlorosilane (FDTS; Gelest Inc., Morrisonville, PA) mixed with anhydrous toluene (Sigma-Aldrich, St. Louis, MO) followed by rinsing with excess toluene after FDTS soak process. Polycarbonate sheets, a readily available bulk, commercial polymer (Menards, Columbus, OH) served as the third substrate. Polycarbonate was obtained with an adhesive-free protective seal and the samples were stored in the sealed dry box used for sample storage till any experiments were conducted. A well-established degrease and cleaning procedure[54,55] was used just prior to imaging nanobubbles on polycarbonate to eliminate any contamination.

Surface Characterization

Contact angle (CA) measurements (Ramé-Hart Goniometer model 250-00), were performed on the substrates using DI water (Millipore, 18.2 MΩ). Data collected includes the average and standard deviation measured from 8 different locations, across each substrate. Surface roughness for each of the three substrates was measured in air using an Asylum Research MFP-3D Bio (Asylum Research, Santa Barbara, California) atomic force microscope (AFM). For liquid measurements, the substrates were initially sonicated in DI water for 15 min in a class 100 cleanroom, dried with a steady nitrogen stream and then placed in a fluid cell.

A recent study[56] showed that using a syringe with metal needle to fill the fluid cell (with water) resulted in PDMS contamination and suggested the use of plastic syringe without a metal cannula. Therefore, in all measurements and subsequent data reported here, the fluid cell was filled with 200 µl of DI water pipetted using a clean, single-use disposable plastic nozzle on a dedicated micropipette.

Tapping mode (TM) measurements were conducted using iDrive triangular silicon nitride cantilevers with Cr/Au reflex coating (resonant frequency ≈ 7-8 KHz in water, cantilever spring constant, k = 0.02 N/m) and 4-sided pyramidal tip with a nominal tip radius of 42 ± 12 nm, as described in the manufacturer specifications and also verified explicitly via scanning electron microscopy.[57] In order to prevent any chance of contamination from the AFM cantilevers, as has been discussed broadly in the past,[56] the cantilever was cleaned by rinsing with copious amounts of acetone, ethanol, and DI water based on previous reported methods.[42] Additionally, imaging experiments (results not shown explicitly) with an UV/Ozone cleaned tip[33] did not show any noticeable difference in UV/Ozone cleaned cantilevers and liquid cleaned cantilevers

for nanobubble imaging. All TM-AFM measurement were conducted after 30 min of filling the liquid cell in order to minimize the time influence on nanobubbles, using information from previous nanobubble reports.[34] The room was maintained at 21 ± 0.5°C during the course of all measurements with minimal temperature impact on the substrate.

Estimation of nanobubble morphology via finite-sized tip correction methodology

TM-AFM images generated by scanning the substrates were analysed to extract information on nanobubble morphology. It is important to note that the radius of curvature of the AFM tip is comparable to the total radius of curvature of nanobubbles reported in this study, which leads to an over-estimation of the actual lateral radius and subsequently the total radius of curvature of the nanobubble[39] (schematic showing nanobubble geometry and dimensions is presented in Figure S1, supporting information). Therefore, in order to estimate accurate nanobubble sizes with minimal uncertainty due to the finite size effects of the AFM cantilever tip, a well-established correction method for finite size tips was implemented.

Briefly, for a given nanobubble, the apparent lateral radius R_s^{app} and height h^{app} i.e., before tip correction, were measured from four different cross-sections (similar to the method reported by Li et al.[27]) to estimate the mean and associated standard deviation. No correction was applied to apparent height[34,39] as only the tip apex was assumed to be used in taking measurements without interference from the tip side walls. This assumption holds true only when the height is smaller than the total radius of curvature, which is the case for all the nanobubbles reported in the present study and therefore $h^{app} = h$.[34,39] The apparent total radius of curvature, R_c^{app} was then evaluated by substituting the extracted mean values (from the four cross-sections) of R_s^{app} and h in equation 1. The tip-corrected total radius of curvature, R_c was then obtained by subtracting the AFM tip radius R_{tip}, (42 nm[57]) from R_c^{app} as shown in equation 2 below.[38] The tip corrected lateral radius, R_s was then determined from equation 3.[39] The uncertainty associated with R_c and R_s were calculated based on the known uncertainty of R_s^{app}, h^{app} (as discussed) and R_{tip}[57] and incorporated using well-known error propagation methods.[58]

$$R_c^{app} = \frac{(R_s^{app})^2 + h^2}{2h} \tag{1}$$

$$R_c = R_c^{app} - R_{tip} \tag{2}$$

$$R_s = \sqrt{2hR_c - h^2} \tag{3}$$

Results and Discussion

Contact angle and Roughness measurements

Advancing, receding, and static contact angles were measured for all three substrates using the sessile drop method and the results are summarized in Table 1. The static contact angle of the substrates varied as: 81.1° ± 1.3° for polycarbonate

Journal Name

ARTICLE

Table 1. Macroscopic contact angle and root mean squared (RMS) roughness measurements for polycarbonate and chemically modified fluoro- and bromo-terminated substrates.

Substrate	Static	Advancing	Receding	Hysteresis	RMS-Roughness
Polycarbonate	81.1° ± 1.3°	88.7° ± 1.0°	77.9° ± 1.7°	10.8°	1.51 ± 0.13 nm
BTS	85.5° ± 0.7°	101.2° ± 1.7°	73.4° ± 2.5°	27.8°	0.72 ± 0.06 nm
FTS	105.3° ± 1.4°	118.3° ± 1.8°	88.9° ± 3.4°	29.4°	1.81 ± 0.27 nm

(hydrophilic), 85.5° ± 0.7° for BTS (hydrophilic) and 105.3° ± 1.4° for FTS (hydrophobic). The macroscopic contact angle hysteresis of chemically modified surfaces i.e. BTS (27.8°), and FTS (29.4°) are almost similar and about 2.6 times that of polycarbonate (10.8°). TM-AFM measurements indicate that FTS has the roughest surface with a root mean squared (RMS) roughness of 1.81 ± 0.27 nm, closely followed by polycarbonate with a root mean squared RMS roughness of 1.51 ± 0.13 nm and finally BTS, showing the least variation in surface roughness (0.72 ± 0.06 nm), as shown in Table 1. A 20 μm x 20 μm scan of all the three substrates is shown in Figure S2 (supporting information) that shows the overall quality of the substrates used in this work.

TM-AFM analysis in air-equilibrated water

Nanobubbles formed on all three substrates were characterized using tapping mode atomic force microscopy (TM-AFM). It is important to note that use of TM-AFM for nanobubble imaging has to be done carefully since a previous report[51] showed that the measured nanobubble size and profile are dependent on the peak force set point in the repulsive tip-sample interaction regime; with less repulsive force, the apparent height and width of nanobubbles are larger. It is well known that the tapping mode scans provide less distortive information for soft surfaces when operated in the attractive force regime.[59] The two regimes (repulsive or attractive) can be easily distinguished by the phase signal in TM-AFM[60] instead of the amplitude set point ratio as it can lead to misinterpretation of results.[51,61] The data reported here was verified for operation in the attractive forces regime with phase shift varying between 90° – 140° using iDrive excitation at cantilever's resonance frequency (Figure S3). Furthermore, the electromagnetic actuation (iDrive)[62,63] ensures a smooth and reliable resonance peak for the micro-cantilever in liquid probing environment, making the phase interpretation easier without ambiguities as compared to acoustic mode excitation in many traditional tapping mode setups that show multiple resonance peaks.[53,62,63]

The tip correction scheme discussed above was applied to all nanobubbles imaged on each of the three substrates, FTS, BTS, and polycarbonate to calculate the mean Laplace pressure (ΔP) associated with nanobubbles on each of the three substrates.

Laplace pressure of a nanobubble is the difference in pressure inside a nanobubble with respect to ambient pressure. Laplace pressure was chosen as the metric for characterization of the nanobubbles as it relates the size of a nanobubble and its relative pressure compared to the surrounding fluid pressure. For a stationary pinned nanobubble, the net external force due to Laplace pressure must be balanced by surface tension acting on it (see Figure S1, supporting information). From the force balance, Laplace pressure is related to R_c as shown in equation 4, where γ_{LV} is the liquid vapor surface tension and is 0.072 N/m for water/air interface.[27,39]

$$\Delta P = 2 \gamma_{LV} R_c^{-1} \qquad (4)$$

Figure 1 shows the TM-AFM topography images and calculated Laplace pressure of surface nanobubbles formed on FTS (Figures 1a and 1b), BTS (Figures 1c and 1d), and polycarbonate (Figures 1e and 1f). The nanobubble images for FTS, BTS, and polycarbonate are shown in Figures 1a, 1c, and 1e respectively with Figures 1b, 1d, and 1f showing the Laplace pressure plotted against R_s along with one standard deviation from the mean for each of these three substrates. As shown in Figure 1, R_s of the nanobubbles were in the range of 90 – 270 nm for FTS, 11 – 27 nm for BTS, and 11 – 22 nm for polycarbonate. The height of the nanobubbles were in the range of 20 – 66 nm for FTS, 4 – 8 nm for BTS, and 5 – 14 nm for polycarbonate. Nanobubble morphology remained constant over the duration of the experiment, which is in agreement with previous reports that show pinned nanobubbles with no changes to morphology when imaged over several hours.[17,33,34,64,65] The cumulative overall uncertainty of R_s^{app}, h^{app} and R_{tip} resulted in a higher relative standard deviation associated with the lateral radius (equation 3), specifically for bubbles with $R_s < 50$ nm, i.e., BTS and polycarbonate (Figure 1 d, f). However, this uncertainty does not impact the trends and conclusions presented in this paper.

The Laplace pressure varied from 0.2 – 0.7 MPa for FTS, 2.5 – 10.3 MPa for BTS, and 4.2 – 9.4 MPa for polycarbonate. The results indicate that nanobubbles formed on BTS (contact angle was 85.5°, Table 1) and polycarbonate (contact angle was 81.1°, Table 1) have a similar range of Laplace pressure and
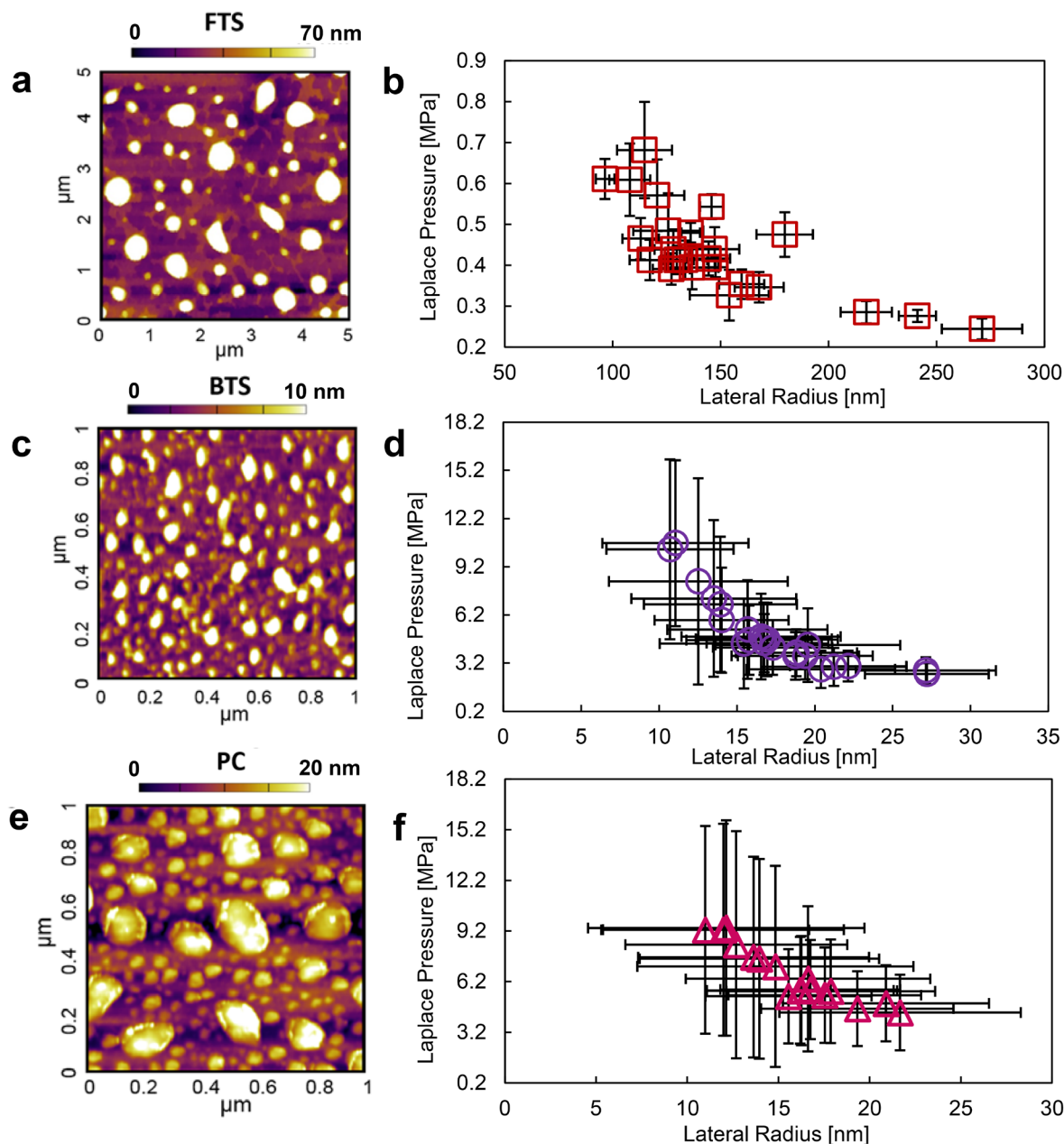
Journal Name

ARTICLE

Figure 1. TM-AFM topography images showing surface nanobubbles as a function of lateral radius, R_s for (a) FTS substrates for a representative 5 µm x 5 µm scan, and (b) corresponding Laplace pressure for the FTS substrate, (c) BTS substrates for a representative 1 µm x 1 µm scan, and (d) corresponding Laplace pressure for the BTS substrate, (e) polycarbonate substrates for a representative 1 µm x 1 µm scan, and (f) corresponding Laplace pressure for polycarbonate substrates when imaged in air-equilibrated water. The Laplace pressure estimated for BTS and polycarbonate were both an order of magnitude higher than that of FTS. The error bars indicate one standard deviation of representative parameters of each nanobubble.

both are an order of magnitude higher than that of FTS (contact angle was 105.3°, Table 1). In order to further compare the Laplace pressures for the nanobubbles observed on the three substrates here, an extensive literature review was conducted to develop a regime map from published reports that showed the

dependence of Laplace pressure as a function of surface hydrophobicity (see Figure S4 and Table S1 in supporting information for additional discussion on regime map). Based on calculated Laplace pressures for the variety of nanobubbles previously reported, three regimes were defined: Regime 1 with

$\Delta P \sim$ O($10^{-2} - 10^{-1}$) MPa; Regime 2 with $\Delta P \sim$ O($10^{-1} - 10^{0}$) MPa; and Regime 3 with $\Delta P \sim$ O($10^{0} - 10^{1}$) MPa. As is evident from Figure S4, no consensus exists in observations of nanobubble size even for the similar substrates that have been studied by numerous past researchers leading to the broad discussion of substrate type, substrate properties, and variability in measurement methods along with subsequent interpretation of data as discussed in the introduction section.

The Laplace pressure of nanobubbles on both BTS and polycarbonate were found to be similar to the nanobubbles formed by the interaction of air-equilibrated water with hydrophilic gold surfaces (contact angle $\approx$ 80°)[39] and hydrophilic self-assembled monolayers of octadecanethiol (ODT)/16-mercaptohexadecanoic acid (MHDA) on gold (contact angle varying between 37°– 86°, Figure S4, supporting information).[34] The size range and the calculated Laplace pressure for nanobubbles formed on FTS agree with the values reported for nanobubbles formed on OTS coated silicon (contact angle $\approx$ 110°)[65] and for those formed on functionalized hydrophobic gold (contact angle 107°).[34] Therefore, one easily observable trend is that the Laplace pressure of nanobubbles formed upon the interaction of air-equilibrated water with hydrophilic substrates (here, BTS and polycarbonate) belong to Regime 3 ($\Delta P \sim$ O($10^{0} - 10^{1}$) MPa) and subsequently moves to Regime 2 ($\Delta P \sim$ O($10^{-1} - 10^{0}$) MPa) as the surfaces become more hydrophobic (here, FTS). As observed in Table 1, FTS and polycarbonate have similar RMS roughness (1.5 – 1.8 nm), but the size of nanobubbles varies by an order of magnitude (Figure 1). Also, the macroscopic contact angle hysteresis was found to be similar between FTS and BTS ($\approx$ 28° – 29°), but the Laplace pressure and conversely the nanobubble size were again found to be different by an order of magnitude (Figure 1). The results here suggest that interfacial nanobubble size is dominated primarily by the macroscopic static contact angle of the substrates.

Contact Line Tension (CLT)

In contrast to a macrobubble suspended in bulk water, interfacial nanobubbles are pinned or attached to the substrate leading to an interface contact line at the gas-solid interface. Previous research[33] shows that this three phase (gas or vapor, liquid, and solid) contact line pinning prevents changes to bubble morphology. Contact line pinning assumes that the lateral width of the bubble remains constant and changes to bubble morphology, and subsequently Laplace pressure, are due to changes in the height of nanobubble.[33] For a three phase system, contact line tension is defined as the excess free energy per unit length along the gas-solid interface.[67]

The modified Young's equation (also called Young-Dupré equation) is used to obtain the three phase contact line tension, τ_{SLV} (equation 5).[68-70]
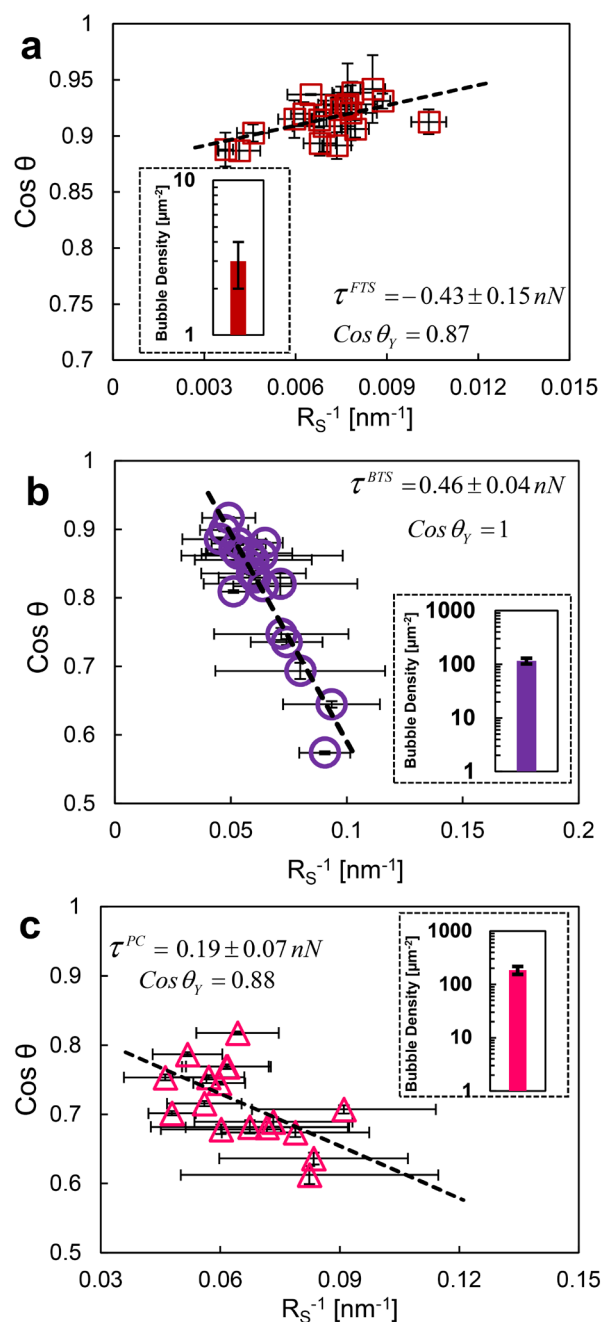

Figure 2. Young-Dupré plot showing the variation of cosine of nanoscopic contact angle (*Cos θ*) with inverse of lateral radius, R_s^{-1} for the nanobubbles formed on a) FTS b) BTS, and c) Polycarbonate for the representative images for nanobubbles shown in figure 1. The inset to each image here shows the nanobubble density for each of the three substrates. The bubble density was found to decrease as the macroscopic contact angle increases from 81.1° for polycarbonate to 105° for FTS. The contact line tension was estimated to be negative for the nanobubbles found on FTS and positive for the relatively smaller nanobubbles observed on BTS and polycarbonate. The error bars indicate one standard deviation of representative parameters of each nanobubble.

$$Cos\ \theta = Cos\ \theta_Y - \frac{\tau_{SLV}}{\gamma_{LV}R_s} \qquad (4)$$

$$\theta = Sin^{-1}(\frac{R_s}{R_c}) \qquad (5)$$

In equations 5 and 6, θ is the nanoscopic gas side contact angle. It is worth noting that the nanoscopic contact angle is distinct from macroscopic static contact angle of water droplets on the substrates reported in Table 1, and θ_Y is the Young's contact angle. The gas side nanoscopic contact angle, along with associated uncertainty was estimated by using a regression analysis after determining the contact angle from the TM-AFM images for multiple nanobubbles on each substrate. θ is plotted against R_s in Figure S5 (see supporting information).

From Figure S5, it is evident that the nanoscopic and macroscopic contact angle (Table 1) are not equal even for nanobubbles with $R_s > 50$ nm, which is in agreement with past work.[31,39,46,71] By contrast, fullerene nanodroplets on silica surfaces[72] show that for sessile drops with droplet radius greater than 20 nm, the contact angles were found to be size independent and equal to the macroscopic contact angle. The difference in the contact angles for nanodroplets and nanobubbles likely occurs because the gas nanobubbles at a given Laplace pressure are pinned to the solid substrate and surrounded by liquid containing dissolved air and a recent study showed that this nanobubble interface is permeable to gas transport, thereby giving rise to a dynamic system affecting the interfacial properties.[73] Furthermore, the mechanism behind the weak size dependence of contact angle for the gas nanobubbles continues to be an open question with one of the hypotheses suggesting that the origins can be attributed to effects due to surface inhomogeneities and surface tension.[46]

Using equation 5, $Cos \theta$ was plotted against the inverse of lateral radius, R_s^{-1} for each of the three substrates as shown in Figures 2a – 2c, where the error bars indicate one standard deviation from the mean for each of the representative parameters. As reported previously, equation 5 does not take into account effects of surface topology on the contact angles,[31] and therefore the overall estimated uncertainty could be larger, but quantification of this additional uncertainty is beyond the scope of this work. τ_{SLV} and $Cos \theta_Y$ were determined using a two parameter least squared fit, using the methods reported previously.[39,71]

CLT was calculated to be -0.43 ± 0.15 nN for the nanobubbles observed on FTS (Figure 2a). Importantly, the magnitude of CLT for FTS falls in the same regime as estimated in several previous reports for other hydrophobic surfaces with R_s of the pinned air bubbles greater than 50 nm.[27,31,39,71,74,75] Physically, a negative line tension acts against the surface tension to expand and flatten the nanobubble[31, 39] leading to a lowering of the Laplace pressure. By contrast, a positive value of CLT was calculated for BTS (0.46 ± 0.04 nN) and polycarbonate (0.19 ± 0.07 nN) ($R_s < 50$ nm for both substrates) with the implication that a positive value of line tension acts in conjunction with surface tension towards nanobubble shrinkage.[39] It is worth noting that molecular dynamics simulations show the challenges in theoretically estimating θ and CLT.[76,77] Therefore, for any experimental data reported, it is important to note the uncertainty in reported CLT values arising due to the finite size

of AFM tip, as described above. As a fraction of the estimated CLT, FTS shows the highest uncertainty with BTS showing the least. Therefore, with the macroscopic contact angle decreasing from 105° for FTS to 81.1° for polycarbonate, the contact line tension changed from negative to positive, within experimental uncertainty as discussed above. In addition, it was observed that the CLT for polycarbonate was less than that of BTS by 2.4 times for ≈ 4° change in the macroscopic contact angle. Furthermore, the force per unit length of contact line tension (estimated from Figure 2) acting across the wetted perimeter of a nanobubble, $2\pi R_s$, was found to be comparable to the effect of nanoscopic contact angle hysteresis. From Figure S5, it was found that the nanoscopic contact angle hysteresis of individual nanobubbles were on the order of 3°, significantly lower than the contact angle hysteresis observed for the macroscale water droplet as summarized in Table 1.

Finally, the nanobubble number density was estimated by counting the number of nanobubbles over the scan areas (as shown in the insets to Figure 2) from a minimum of 3 different scans for each substrate, which also confirmed the reproducibility of the study. The nanobubble number density is defined as the total number of nanobubbles per μm^2. The bubble density for FTS, BTS, and polycarbonate were estimated to be 3 ± 1, 115 ± 14, 186 ± 32 per μm^2 respectively. Therefore, the nanobubble density was found to decrease with an increase in macroscopic static contact angle of the substrates (as seen in Table 1). The nanobubble number density observed for the three substrates are also similar to several published reports of other surfaces with similar macroscopic contact angles.[3,4,78]

TM-AFM analysis after solvent exchange

The solvent exchange process or method has been extensively used to generate nanobubbles[35,45,79] and has also been adopted here to introduce super-saturated nanobubbles at the interface for the polycarbonate substrate. The choice of polycarbonate (contact angle ~ 81°) is due to the fact that polycarbonate is a readily available bulk substrate with many practical uses and provides competing information against other extensively used bulk substrates such as polystyrene (average reported contact angle ≈ 95°) and HOPG (reported contact angle ≈ 63° – 90°) for nanobubble studies.

Figure 3a shows the bubble distribution on polycarbonate when the fluid cell was filled with air-equilibrated water for a 5 μm x 5 μm scan area for polycarbonate. Figure 3b shows the height profile of nanobubbles on polycarbonate after performing solvent exchange with water-ethanol-water displacement over the same size scan. Comparing Figure 3a and 3b, it is visually evident that the lateral radius of nanobubbles increased from 12 – 63 nm to 100 – 270 nm and the height increased from 5 – 14 nm to 9 – 26 nm following the solvent exchange process. In contrast, the number density changed from over 180 nanobubbles/μm² to ≈ 3 nanobubbles/μm², as shown in Figure 3d. The Laplace pressure was found to be between 0.1 – 0.25 MPa (Figure 3d) after solvent-exchange,
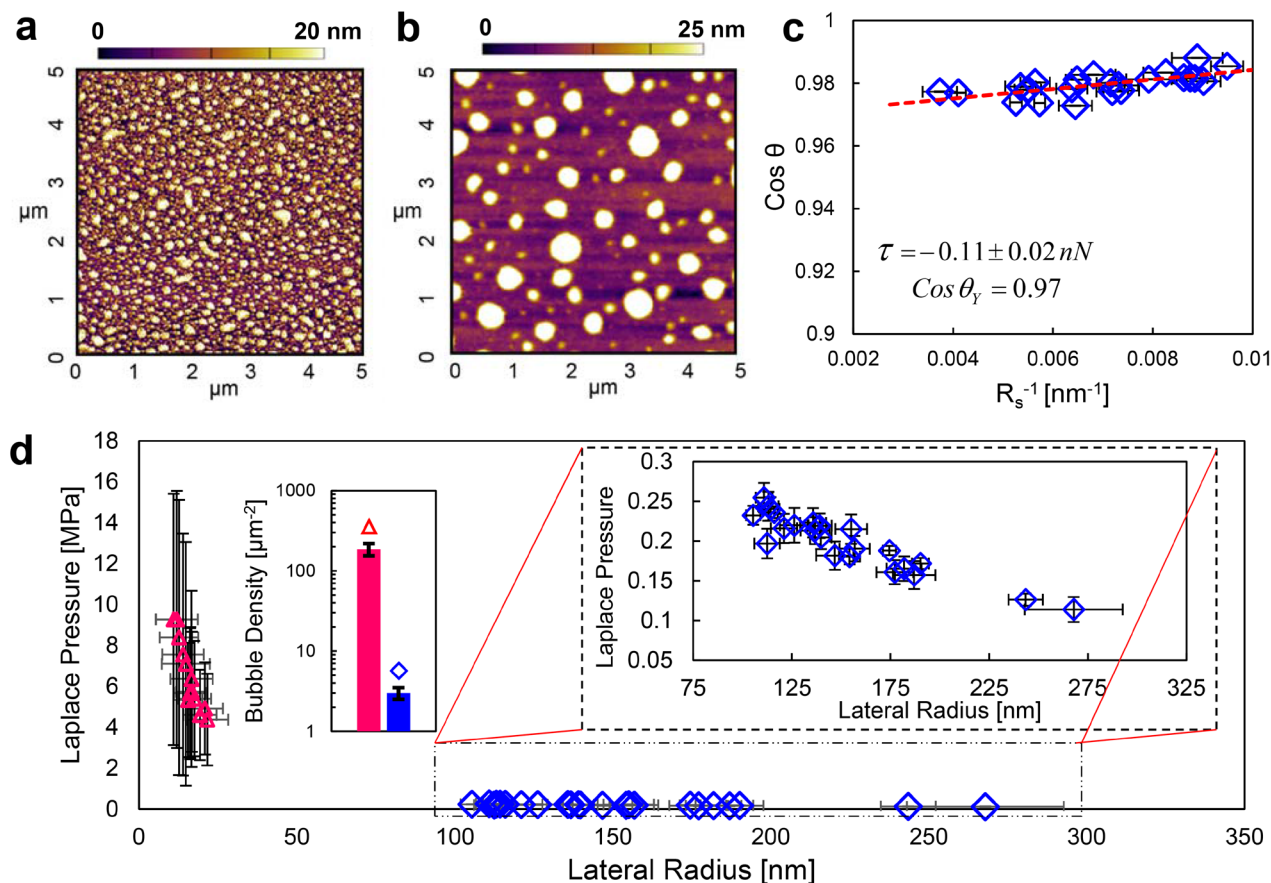
Journal Name

ARTICLE

Figure 3. TM-AFM images of polycarbonate imaged in (a) air-equilibrated water (b) after ethanol exchange, (C) Young-Dupré plot for estimating CLT, (d) Laplace pressure and nanobubble density comparison of polycarbonate before (Δ) and after (◊) ethanol exchange with inset showing magnified view of Laplace pressure of nanobubbles after ethanol exchange. The Laplace pressure decreases by an order of magnitude accompanied by an inversion in the sign of CLT after ethanol exchange. The error bars indicate one standard deviation of representative parameters of each nanobubble.

which is an order of magnitude lower than that of the saturated nanobubbles observed on polycarbonate when imaged in air-equilibrated water (Figure 1f). Additionally, it was found that the CLT changed sign and magnitude from 0.19 ± 0.07 nN to -0.11 ± 0.02 nN (Figure 3c) after solvent exchange. Therefore, depending on the gas saturation in the imaging fluid, the CLT either tries to shrink or expand the nanobubbles to keep the bubble-liquid system in a state of minimal Gibbs energy,[39,80,81] thus giving rise to contrasting dynamics on the same substrate.

Summary and Conclusions

Surface nanobubbles were imaged on two borosilicate glass substrates modified by silane-chemistry to yield bromo- and fluoro-terminated surfaces in addition to a bulk polymeric substrate, polycarbonate. The macroscopic static water contact angle for the substrates varied from $\approx 81°$ to $105°$ thus presenting a pathway to compare the effects of both hydrophilic

and hydrophobic surfaces on nanobubble size and number density. Lateral surface radius and height of the nanobubbles were measured with corrections for finite tip radius and used to calculate nanobubble Laplace pressure and contact line tension. The tapping mode AFM images in the attractive force regime also allowed estimation of nanobubble number density on each substrate.

For nanobubbles formed in air-equilibrated water, the Laplace pressure of nanobubbles formed on BTS and polycarbonate were $\sim O(10^1)$ MPa and were found to be an order of magnitude higher compared to FTS. Also, the nanobubble number density on the substrates was found to decrease from 186 ± 32 for polycarbonate to 3 ± 1 for FTS, with BTS lying between the two extremes at 115 ± 14. Therefore, decreases in nanobubble number density and Laplace pressure were observed with increasing macroscopic static water contact angle for the substrate. Additionally, the magnitude of the contact line

tension was observed to be positive with quantified experimental uncertainty for substrates where all the nanobubbles had a lateral radius less than 50 nm.

Upon imaging the polycarbonate substrate after solvent exchange, the Laplace pressure of the nanobubbles reduced by an order of magnitude and the nanobubble number density decreased from greater than $180/\mu m^2$ to $\approx 3/\mu m^2$. The reduction in Laplace pressure was accompanied by an increase in the lateral surface radius leading to a negative contact line tension, which changed from 0.19 ± 0.07 nN to -0.11 ± 0.02 nN. Therefore, depending on the air-saturation in a given solvent, it is indeed possible to generate nanobubbles of contrasting size, density, and contact line tension.

Acknowledgements

Notes and references

[a] Department of Mechanical and Aerospace Engineering, The Ohio State University, Columbus, OH 43210, United States.
[b] Center for Affordable Nanoengineering of Polymeric Biomedical Devices, The Ohio State University, Columbus, OH 43210, United States.
[c] Department of Engineering Physics, University of Wisconsin – Platteville, Platteville WI 53818, United States.
[*] wuy@uwplatt.edu, prakash.31@osu.edu.

Electronic Supplementary Information (ESI) available: Nanobubble free-body diagram with nomenclature (Figure S1), TM-AFM air scan of FTS, BTS, Polycarbonate (Figure S2), Height/Phase plot of nanobubbles formed with air-equilibrated water on polycarbonate (Figure S3), Literature review summary of Laplace pressure based regime map discussion (Figure S4), Variation of nanoscopic contact angle with lateral radius of nanobubble (Figure S5), Regime Map reference Table (Table S1). See DOI: 10.1039/b000000x/

1. L. Zhang, X. Zhang, C. Fan, Y. Zhang and J. Hu, *Langmuir*, 2009, **25**, 8860-8864.
2. M. A. Hampton and A. V. Nguyen, *Minerals Engineering*, 2009, **22**, 786-792.
3. Y. Wang, B. Bhushan and A. Maali, *Journal of Vacuum Science and Technology A: Vacuum, Surfaces and Films*, 2009, **27**, 754-760.
4. B. Bhushan, Y. Pan and S. Daniels, *Journal of Colloid and Interface Science*, 2013, **392**, 105-116.
5. Y. Pan and B. Bhushan, *Journal of Colloid and Interface Science*, 2013, **392**, 117-121.
6. S. A. Kondrat'ev and N. P. Moshkin, *J Min Sci*, 2014, **50**, 780-787.
7. V. Belova, M. Krasowska, D. Wang, J. Ralston, D. G. Shchukin and H. Mohwald, *Chemical Science*, 2013, **4**, 248-256.
8. H. Yang, W. Cai, L. Xu, X. Lv, Y. Qiao, P. Li, H. Wu, Y. Yang, L. Zhang and Y. Duan, *Biomaterials*, 2015, **37**, 279-288.
9. Z. Wu, H. Chen, Y. Dong, H. Mao, J. Sun, S. Chen, V. S. J. Craig and J. Hu, *Journal of Colloid and Interface Science*, 2008, **328**, 10-14.
10. P. Ball, *ChemPhysChem*, 2012, **13**, 2173-2177.
11. M. A. Hampton and A. V. Nguyen, *Advances in Colloid and Interface Science*, 2010, **154**, 30-55.
12. S. Ljunggren and J. C. Eriksson, *Colloids and Surfaces A: Physicochemical and Engineering Aspects*, 1997, **129–130**, 151-155.
13. J. C. Eriksson and S. Ljunggren, *Colloids and Surfaces A: Physicochemical and Engineering Aspects*, 1999, **159**, 159-163.
14. X. H. Zhang, A. Quinn and W. A. Ducker, *Langmuir*, 2008, **24**, 4756-4764.
15. P. A. Kralchevsky, *Langmuir*, 1996, **12**, 5951-5955.
16. A. Agarwal, W. J. Ng and Y. Liu, *Chemosphere*, 2011, **84**, 1175-1180.
17. Y. Liu and X. Zhang, *The Journal of Chemical Physics*, 2013, **138**, 014706.
18. X. Zhang, M. H. Uddin, H. Yang, G. Toikka, W. Ducker and N. Maeda, *Langmuir*, 2012, **28**, 10471-10477.
19. P. Attard, *Advances in Colloid and Interface Science*, 2003, **104**, 75-91.
20. S. F. Jones, G. M. Evans and K. P. Galvin, *Advances in Colloid and Interface Science*, 1999, **80**, 27-50.
21. H. Peng, M. A. Hampton and A. V. Nguyen, *Langmuir*, 2013, **29**, 6123-6130.
22. M. P. Brenner and D. Lohse, *Physical Review Letters*, 2008, **101**, 214505.
23. S. M. Dammer and D. Lohse, *Physical Review Letters*, 2006, **96**, 206101.
24. X. H. Zhang, A. Khan and W. A. Ducker, *Physical Review Letters*, 2007, **98**, 136101.
25. M. Mezger, S. Schöder, H. Reichert, H. Schröder, J. Okasinski, V. Honkimäki, J. Ralston, J. Bilgram, R. Roth and H. Dosch, *The Journal of Chemical Physics*, 2008, **128**, 244705.
26. D. Lohse and X. Zhang, *Physical Review E*, 2015, **91**, 031003.
27. D. Li, D. Jing, Y. Pan, W. Wang and X. Zhao, *Langmuir*, 2014, **30**, 6079-6088.
28. A. C. Simonsen, P. L. Hansen and B. Klösgen, *Journal of Colloid and Interface Science*, 2004, **273**, 291-299.
29. A. Agrawal, J. Park, D. Y. Ryu, P. T. Hammond, T. P. Russell and G. H. McKinley, *Nano Letters*, 2005, **5**, 1751-1756.
30. Y. Wang, B. Bhushan and X. Zhao, *Langmuir*, 2009, **25**, 9328-9336.
31. J. Yang, J. Duan, D. Fornasiero and J. Ralston, *The Journal of Physical Chemistry B*, 2003, **107**, 6139-6147.
32. J. W. G. Tyrrell and P. Attard, *Langmuir*, 2002, **18**, 160-167.
33. X. Zhang, D. Y. C. Chan, D. Wang and N. Maeda, *Langmuir*, 2013, **29**, 1017-1023.
34. B. Song, W. Walczyk and H. Schönherr, *Langmuir*, 2011, **27**, 8223-8232.
35. X. H. Zhang, N. Maeda and V. S. J. Craig, *Langmuir*, 2006, **22**, 5025-5035.
36. B. M. Borkent, S. de Beer, F. Mugele and D. Lohse, *Langmuir*, 2009, **26**, 260-268.

37. S. Prakash, M. B. Karacor and S. Banerjee, *Surface Science Reports*, 2009, **64**, 233-254.

38. S. Yang, S. M. Dammer, N. Bremond, H. J. W. Zandvliet, E. S. Kooij and D. Lohse, *Langmuir*, 2007, **23**, 7072-7077.

39. N. Kameda and S. Nakabayashi, *Chemical Physics Letters*, 2008, **461**, 122-126.

40. M. Holmberg, A. Kühle, K. A. Mørch and A. Boisen, *Langmuir*, 2003, **19**, 10510-10513.

41. Y. Chih-Wen, L. Yi-Hsien and H. Ing-Shouh, *Journal of Physics: Condensed Matter*, 2013, **25**, 184010.

42. X. H. Zhang, X. Zhang, J. Sun, Z. Zhang, G. Li, H. Fang, X. Xiao, X. Zeng and J. Hu, *Langmuir*, 2006, **23**, 1778-1783.

43. B. Zhao, Y. Song, S. Wang, B. Dai, L. Zhang, Y. Dong, J. Lu and J. Hu, *Soft Matter*, 2013, **9**, 8837-8843.

44. R. P. Berkelaar, H. J. W. Zandvliet and D. Lohse, *Langmuir*, 2013, **29**, 11337-11343.

45. S. Lou, J. Gao, X. Xiao, X. Li, G. Li, Y. Zhang, M. Li, J. Sun, X. Li and J. Hu, *Materials Characterization*, 2002, **48**, 211-214.

46. C. Xu, S. Peng, G. G. Qiao, V. Gutowski, D. Lohse and X. Zhang, *Soft Matter*, 2014, **10**, 7857-7864.

47. T. Nishiyama, Y. Yamada, T. Ikuta, K. Takahashi and Y. Takata, *Langmuir*, 2015, **31**, 982-986.

48. R. Raj, S. C. Maroo and E. N. Wang, *Nano Letters*, 2013, **13**, 1509-1515.

49. H. Yang, S.-Y. Fung, M. Pritzker and P. Chen, *PLoS ONE*, 2007, **2**, e1325.

50. Y. J. Shin, Y. Wang, H. Huang, G. Kalon, A. T. S. Wee, Z. Shen, C. S. Bhatia and H. Yang, *Langmuir*, 2010, **26**, 3798-3802.

51. W. Wiktoria, M. S. Peter and S. Holger, *Journal of Physics: Condensed Matter*, 2013, **25**, 184005.

52. S. Prakash, T. M. Long, J. C. Selby, J. S. Moore and M. A. Shannon, *Anal. Chem.*, 2007, **79**, 1661-1667.

53. Y. Wu, S. Misra, M. B. Karacor, S. Prakash and M. A. Shannon, *Langmuir*, 2010, **26**, 16963-16972.

54. S. Prakash and M. B. Karacor, *Nanoscale*, 2011, **3**, 3309-3315.

55. T. M. Long, S. Prakash, M. A. Shannon and J. S. Moore, *Langmuir*, 2006, **22**, 4104-4109.

56. R. P. Berkelaar, E. Dietrich, G. A. M. Kip, E. S. Kooij, H. J. W. Zandvliet and D. Lohse, *Soft Matter*, 2014, **10**, 4947-4955.

57. A. Research. http://www.asylumresearch.com/Probe/BL-TR400PB.

58. R. Figliola and D. Beasley, *Theory and Design for Mechanical Measurements,*, Fifth Edition edn., John Wiley and Sons, 2010.

59. R. W. Stark, G. Schitter and A. Stemmer, *Physical Review B*, 2003, **68**, 085401.

60. R. García and A. San Paulo, *Physical Review B*, 1999, **60**, 4961-4967.

61. W. Walczyk and H. Schönherr, *Langmuir*, 2014, **30**, 11955-11965.

62. I. Revenko and R. Proksch, *Journal of applied physics*, 2000, **87**, 526-533.

63. X. Xu and A. Raman, *Journal of Applied Physics*, 2007, **102**, 034303.

64. J. H. Weijs and D. Lohse, *Physical Review Letters*, 2013, **110**, 054501.

65. B. Bhushan, Y. Wang and A. Maali, *Journal of Physics: Condensed Matter*, 2008, **20**.

66. N. Ishida, T. Inoue, M. Miyahara and K. Higashitani, *Langmuir*, 2000, **16**, 6377-6380.

67. J. H. Weijs, A. Marchand, B. Andreotti, D. Lohse and J. H. Snoeijer, *Physics of Fluids (1994-present)*, 2011, **23**, -.

68. J. Drelich and J. D. Miller, *Particulate Science and Technology*, 1992, **10**, 1-20.

69. J. Drelich and J. D. Miller, *Journal of Colloid and Interface Science*, 1994, **164**, 252-259.

70. J. Gaydos and A. W. Neumann, *Journal of Colloid and Interface Science*, 1987, **120**, 76-86.

71. W. Guo, H. Shan, M. Guan, L. Gao, M. Liu and Y. Dong, *Surface Science*, 2012, **606**, 1462-1466.

72. J. K. Berg, C. M. Weber and H. Riegler, *Physical Review Letters*, 2010, **105**, 076103.

73. S. R. German, X. Wu, H. An, V. S. J. Craig, T. L. Mega and X. Zhang, *ACS Nano*, 2014, **8**, 6193-6201.

74. M. A. J. van Limbeek and J. R. T. Seddon, *Langmuir*, 2011, **27**, 8694-8699.

75. J. Drelich, J. L. Wilbur, J. D. Miller and G. M. Whitesides, *Langmuir*, 1996, **12**, 1913-1922.

76. H. Peng, G. R. Birkett and A. V. Nguyen, *Molecular Simulation*, 2013, **40**, 934-941.

77. H. Peng, A. V. Nguyen and G. R. Birkett, *Molecular Simulation*, 2012, **38**, 945-952.

78. B. Bhushan, Y. Wang and A. Maali, *Langmuir*, 2009, **25**, 8117-8121.

79. S.-T. Lou, Z.-Q. Ouyang, Y. Zhang, X.-J. Li, J. Hu, M.-Q. Li and F.-J. Yang, *Journal of Vacuum Science & Technology B*, 2000, **18**, 2573-2575.

80. H. Y. Erbil, *Surface Science Reports*, 2014, **69**, 325-365.

81. L. Boruvka and A. W. Neumann, *The Journal of Chemical Physics*, 1977, **66**, 5464-5476.

Soft Matter Accepted Manuscript